Micron 109 (2018) 22–33

Contents lists available at ScienceDirect

Micron

journal homepage: www.elsevier.com/locate/micron

Petrographic characterization to build an accurate rock model using micro-CT: Case study on low-permeable to tight turbidite sandstone from Eocene Shahejie Formation

Muhammad Jawad Munawar[a], Chengyan Lin[a,b,*], Veerle Cnudde[c], Tom Bultreys[c], Chunmei Dong[a,b], Xianguo Zhang[a,b], Wesley De Boever[c], Muhammad Aleem Zahid[a], Yuqi Wu[a]

[a] School of Geosciences, China University of Petroleum, Qingdao, 266580, PR China
[b] Key Laboratory of Reservoir Geology in Shandong Province, Qingdao, 266580, PR China
[c] Department of Geology, PProGRess/UGCT, Ghent University, Krijgslaan 281-S8, 9000, Ghent, Belgium

ARTICLE INFO

Keywords:
Pore network model (PNM)
Macropores
Micropores
Micro-CT
Tight sandstone

ABSTRACT

Pore scale flow simulations heavily depend on petrographic characterizing and modeling of reservoir rocks. Mineral phase segmentation and pore network modeling are crucial stages in micro-CT based rock modeling. The success of the pore network model (PNM) to predict petrophysical properties relies on image segmentation, image resolution and most importantly nature of rock (homogenous, complex or microporous). The pore network modeling has experienced extensive research and development during last decade, however the application of these models to a variety of naturally heterogenous reservoir rock is still a challenge. In this paper, four samples from a low permeable to tight sandstone reservoir were used to characterize their petrographic and petrophysical properties using high-resolution micro-CT imaging. The phase segmentation analysis from micro-CT images shows that 5–6% microporous regions are present in kaolinite rich sandstone (E3 and E4), while 1.7–1.8% are present in illite rich sandstone (E1 and E2). The pore system percolates without micropores in E1 and E2 while it does not percolate without micropores in E3 and E4. In E1 and E2, total MICP porosity is equal to the volume percent of macrospores determined from micro-CT images, which indicate that the macropores are well connected and microspores do not play any role in non-wetting fluid (mercury) displacement process. Whereas in E3 and E4 sandstones, the volume percent of micropores is far less (almost 50%) than the total MICP porosity which means that almost half of the pore space was not detected by the micro-CT scan. PNM behaved well in E1 and E2 where better agreement exists in PNM and MICP measurements. While E3 and E4 exhibit multiscale pore space which cannot be addressed with single scale PNM method, a multiscale approach is needed to characterize such complex rocks. This study provides helpful insights towards the application of existing micro-CT based petrographic characterization methodology to naturally complex petroleum reservoir rocks.

1. Introduction

Low permeable and tight sandstone reservoir exhibits porosity and permeability which are subsequent results of depositional and complex diagenetic processes (Golab et al., 2010; Knackstedt et al., 2013). Variable grain size, grain packing, sorting, clay distribution and after burial compaction create highly complex pore spaces (Marquez Ceballos et al., 2014; Solling et al., 2014; Teles et al., 2016). Due to multiscale features, the pores are not uniformly distributed unlike ideal sedimentation models. These micro structures show variable character at multiple scales thus it is challenging to study pore space and fluid flow behavior in these naturally heterogeneous reservoir rocks. (Arns, 2004; Bultreys et al., 2016b; De Boever et al., 2015; Knackstedt and Arns, 2007). Conventional lab analyses, such as pore size distribution (PSD) and capillary pressure are mostly based on either experimental relations or idealized models which are often over simplified to represent rock's complex pore system. Numerous microscopic methodologies and techniques exist to label texture and fabric of rock. Most of them only examine the two-dimensional surface of rock. However, a high-resolution 3D representation of mineral and pore phase can better help to understand the mechanisms that govern fluid flow (Andra et al., 2013). 3D rock models containing spatial arrangements of pore and throats can be generated from micro-CT images. Micro-CT is one of the emerging technique, which can deliver 3D high-resolution images of

* Corresponding author at: School of Geosciences, China University of Petroleum, Qingdao, 266580, PR China.
E-mail address: ycdzycms2017@126.com (C. Lin).

https://doi.org/10.1016/j.micron.2018.02.010
Received 18 December 2017; Received in revised form 24 February 2018; Accepted 25 February 2018
Available online 26 March 2018
0968-4328/

rocks. It provides 3D imaging via X-ray tomography over a continuous length scale of rocks (Cnudde and Boone, 2013; Bultreys et al., 2015). It offers a reliable and non-destructive method to image rock's micro structures up to submicron scale. Resulting 3D digital images from micro-CT can be used for modeling important petrophysical properties (porosity, permeability, formation factor, etc). Two-phase or even three-phase flow which are difficult and time-consuming lab experiments are possible to compute numerically on micro-CT based 3D rock models (Valvatne and Blunt, 2004; Piri and Blunt, 2005). Furthermore, simulations can be run at multiple times with variety of parameters and condition. However, micro-CT imaging has certainly some limitations concerning sample size and resolution. It is reliable to captures micron scale features, whereas it is not possible for micro-CT to capture nanometer scale features. Tight rocks such as limestone and clayey sandstone which exhibit submicron scale pores which cannot be resolved in micro-CT images. In this paper, the term microporosity refers to the pore space which cannot be resolved by microCT.

There are several approaches in practice to segment pore space from micro-CT images, where the resolved pore space (macroporosity) is usually a function of the image resolution. However, morphological and mathematical algorithms can be used to segment and measure microporous regions (Bultreys et al., 2016a; Cid et al., 2017). Characterizing and representing real pore geometry in microporous regions is a difficult computation and numerical task in micro-CT images. However, the influence of microporosity on petrophysical rock properties can be assessed in a rock model (Mehmani and Prodanović, 2014a,b).

After segmentation, single-phase flow can be computed successfully directly on 3D images (Manwart et al., 2002), but pore network models (PNM) are regarded reliable in predicting capillary-controlled multiphase flow (Dong and Blunt, 2009; Bultreys et al., 2016a). In PNM, the pore space is represented in simplified form as a network of connected pores and throats. PNM are being widely deployed to compute macroscopic petrophysical properties such as capillary pressure and relative permeabilities for two (Valvatne and Blunt, 2004) and three-phase (Piri and Blunt, 2005) three-phase fluid flow. Usually, most of the previous PNM studies focus on development with methodological aspects (Bultreys et al., 2016b). The samples used in these studies are regarded as industry standards and their properties are well known. A few studies report on the application of these developments in naturally heterogeneous rocks.

In this paper, we adapted a petrographic approach which integrates image segmentation and a grain recognition-based pore network method which follows percolation theory to characterize petrophysical properties of low permeable to tight Es3 sandstone reservoir from Dongying Depression. We choose four representative samples from Eocene Es3 sandstone reservoir from Dongying Depression based on preliminary thin section. We segment the micro-CT images and extracted PNM, following this absolute permeability is calculated on PNM and directly 3D voxelized micro-CT images by applying Darcy's law. The results are compared to check whether PNM captured enough heterogeneity details of rock. Results from micro-CT based images analysis such as mineral phase segmentation, and PNM data are compared with X-ray diffraction (XRD) analysis and Mercury Injection Capillary Pressure (MICP) data respectively to check the validity of model and its implication for petroleum reservoir.

2. Geological setting

Sandy turbidities generated by sediment gravity flow are regarded as good hydrocarbon reservoirs (Bouma, 2000; Shanmugam, 2002). Marine deep water turbidites have gained huge significance and emphasis globally after recent hydrocarbon discoveries however, little research is published about lacustrine turbidites (Zhang, 2004). Turbidite sandstones are largely formed under lacustrine environments in Dongying depression, located on the south-eastern margin of Jiyang sub-basin which is a division of Bohai Bay Basin, eastern China (Fig. 1a). Es3 is the third member from Eocene Shahejie Formation which is mainly composed of lacustrine turbidites (Fig. 1b). It is a northeast southwest trending basin formed as a result of a Cenozoic rift event (Feng et al., 2013).

During the deposition of third member (ES3) of Shahejie Formation, the sedimentation and accommodation space was controlled primarily by active rifting. Active normal faulting triggered unstable delta front sediments and deposited them in deep water settings as lacustrine turbidites in the Dongying depression (Wang et al., 2013). In Dongying depression, the lacustrine turbidite sandstone consists mainly of dark gray oil bearing fine-grained sandstone, gray sandy mudstone, gray siltstone and mudstone (Liu et al., 2017). Modern exploration activities from 1996 to 2001 have discovered 438 million bbls of oil reserves in turbidite reservoirs of Jiyang sub-basin (Zhang, 2004). These discoveries reflect high potential of lacustrine turbidites reservoir in future exploration.

3. Material and methods

3.1. Samples

Five characteristic turbidite lithofacies were identified from two areas of the Dongying Depression. The facies are: (1) Massive sandstones; (2) Mudclast rich muddy Sandstone; (3) Carbonaceous clasts rich sandstone; (4) Laminated fine sandstone or siltstone and (5) Hemiplegic mudstone. Four characteristic samples were selected from three representative facies (Table 1). These samples were selected based on mineralogical and textural features. Mother samples were collected from drilled cores of four different wells with a core diameter of 10 cm. A detailed summary of the samples, their facies, and dimensions is present in Table 1. The study area and well locations are marked in the location map (Fig. 1a,b). Trims, cuttings and plugs are extracted from same four mother samples for SEM, XRD and MICP analysis respectively.

3.2. Methods

3.2.1. Transmitted light microscopy

The initial study of thin sections was carried out on 36 samples from low permeable to tight reservoir zone of ES3 to categorize textural features and select representative samples for micro-CT experiment. Samples were mounted on a glass plate with glue and polished down to 0.03 mm. Thin sections were impregnated with blue epoxy to capture the porosity. For carbonate mineral identification, Alizarin red S and K-ferricyanide were used to partly stain the thin sections. These thin sections were examined using a Zeiss Axioscope optical microscope under transmitted light using both plain polarized and cross-polarized light.

3.2.2. Scanning electron microscope (SEM)

Scanning electron microscope (Philips-FEI Quanta 200) unit present at Shingli Oil field research labs (Dongying) was used in this study to acquire submicron resolution to observe clay minerals and microporosity present in clay and dissoluted feldspar. We extracted trims on adjacent locations of micro-CT plugs from mother samples (Table 1) for SEM microscopy. The surfaces of the trims were coated with gold and platinum to avoid electron charging effect in the SEM images.

3.2.3. X-ray diffraction

X-ray diffraction (XRD) analysis was performed to characterize the mineral content on sister samples extracted from mother samples (Table 1) and to find out the bulk mineralogy which could be compared with the mineral phase volumes segmented in micro-CT images. The samples were dried and ground to powder; fifty grams of powdered sample was used for XRD analysis. The mineral content was measured using the D500 X-ray diffractometer with Ni filtered Cu-Ka radiation,

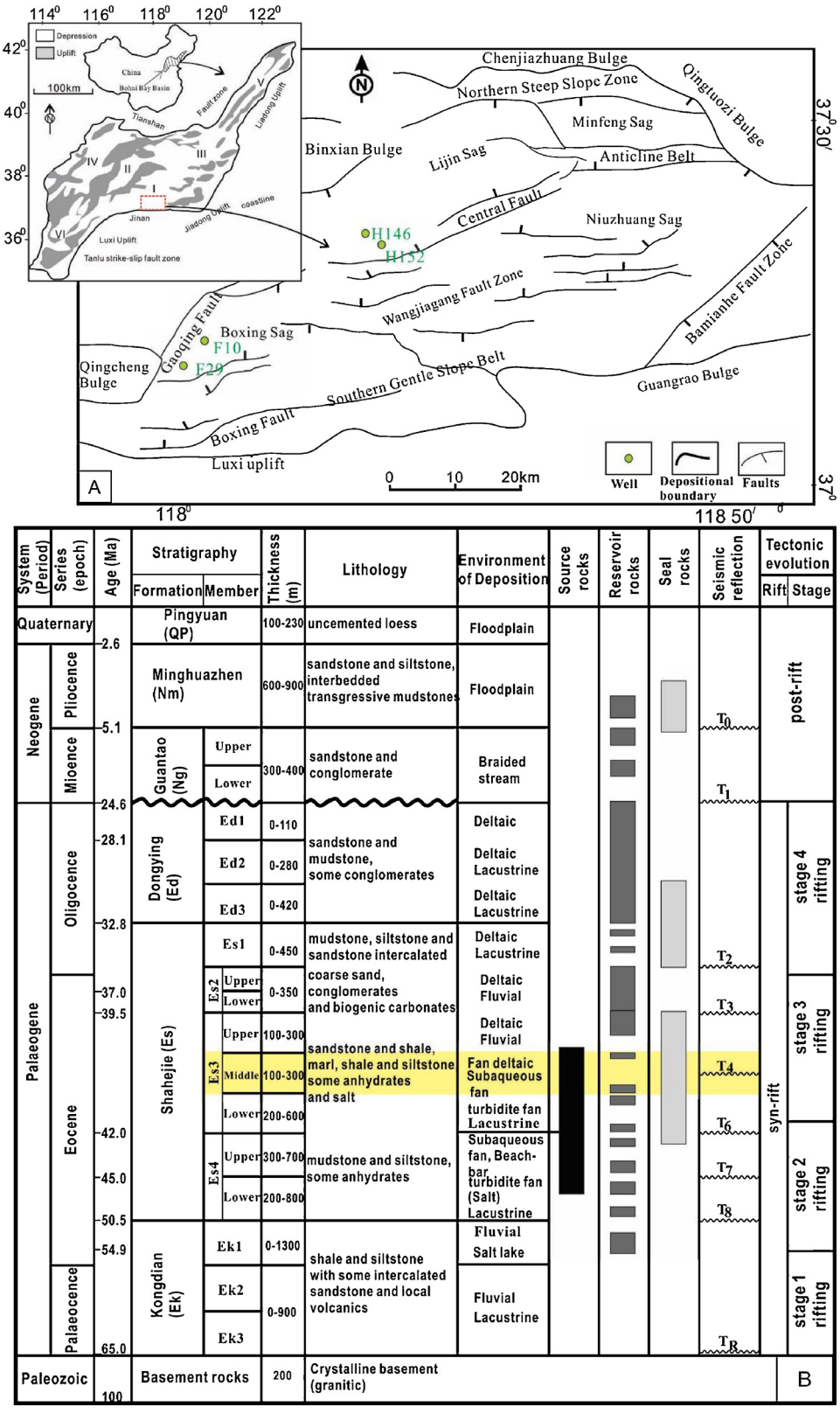

Fig. 1. (A) Stratigraphic chart showing target Es3 interval from the Eocene Shahejie Formation; (B) Map showing the location of the study area in the Dongying Depression.

the copper tube was operated at 40-kV beam energy and 100-mA beam current. Rietveld method was used to find out bulk mineralogy of the samples.

3.2.4. Micro-CT

As the resolution of the micro-CT imaging, is influenced by the sample diameter. The plugs diameters were purely selected keeping in view the scale of the microstructure (grain size and pore size) present in

Table 1
List of samples with corresponding information such as well name, depth, facies and sample dimensions used for SEM and micro-CT.

Sample	Well	Depth (m)	Facies/Assciations	Plug			Sub-plug		
				Diameter (mm)	Length (mm)	Voxel Size (μm)	Diameter (mm)	Length (mm)	Voxel Size (μm)
E1	F10	2890	Massive sandstone/Turbidite Channel	5	7	4.63	2	4	1.49
E2	F29	2869	Massive sandstone/Turbidite channel	5	6	4.92	2	4	1.49
E3	H152	3083	Laminated sandstone/Turbidite lobe	4	5	2.99	3	3	1.7
E4	H146	3090	Carbonaceous clast rich sandstone/Turbidite lobe	4	6	2.99	1	3	1.7

that particular sample to scan the samples at an optimal micro-CT image resolution. In the first stage of the workflow, 5 mm plugs for E1 and E2 and 4 mm plugs for E3 and E4 were extracted from mother core samples. E1, E2, E3 and E4 plugs were scanned at resolution of 4.63., 4.92, 2.99 and 2.99 μm respectively using the micro-CT scanner HECTOR (Masschaele et al., 2013) to visualize and understand heterogeneity of these samples. Then, 3 mm sub-plug for E3, 2 mm sub-plugs for E1 and E2 and 1 mm sub-plug for E4 were extracted for high-resolution scanning. The high-resolution micro-CT scans were performed on E1, E2, E3 and E4 sub-plugs using UGCT's MEDUSA. MEDUSA is the re-designed version of the first UGCT sub-micron CT system, of which a description can be found in Masschaele et al. (2013). Both HECTOR and MEDUSA are custom built micro-CT scanners by Ghent University Centre for X-ray Tomography (UGCT, www.ugct.ugent.be) to achieve the desired image resolution for a variety of materials combined with high image quality. The sample size and acquired voxel size for each image is presented in Table 1.

Octopus Reconstruction software (XRE, Belgium) was used for tomographic reconstruction of 3D images. Maximum sized cubes inscribing cylindrical samples were cropped. These 3D images were filtered with non-local means filter to reduce noise and preserve the pore space. Following this, the datasets were segmented into multiphase 3D images by applying watershed segmentation (Schlüter et al., 2014) present in Avizo software (FEI). After segmentation, the images were processed with common filters and thinning operations to eliminate artefacts using Octopus Analysis (XRE, Belgium) software.

Following this, the pore network was extracted using Ecore software (FEI) the grain recognition-based method by Bakke and Øren (1997). This method identifies grains in a 3D segmented image of rock, using maximum inscribed circles that can be drawn inside a cluster of grain voxels. Then the grains are dilated until there is no pore space left. Connection of three grains represent links (throats), while four or more grains junction represent nodes (pore) location in the network (Bakke and Øren, 1997). This PNM follow percolation theory and a percolation porosity can be calculated via this method.

Absolute permeability was calculated directly on 3D segmented voxelized images with a finite volume method by solving Stokes equations and applying the Darcy's law. The simulations were performed using FEI-Avizo software. A single-phase incompressible Newtonian fluid with a steady-state laminar flow and a viscosity of 0.001 Pa s is considered for simulation. Input pressure boundary conditions are set as 130 KPa and output as 100 KPa.

3.2.5. MICP

Standard MICP can estimate pore-throat size between 30 nm and 200 mm, while high-pressure MICP can detect pores-throats up to 3 nm (Cao et al., 2016a,b). In this study, we used high pressure MICP to measure pore size down to nanometer scale. Mercury is a non-wetting fluid and thus does not penetrate pores by the capillary action until and unless by the application of external pressure. MICP measurements is the standard method and an acceptable approach for characterizing pore features, particularly pore throat distributions in porous media from the micron scale to the nano-scale (Elgmati and Bai, 2011; Ortega and Aguilera, 2014). As the volume of mercury entering into the certain pore size is a function of the applied pressure, pressure versus volume data obtained from MICP provides a way to characterize pore-throat distribution (Cao et al., 2016a,b). 6 mm sister plugs were extracted from each mother sample (Table 1) for MICP experiment. The experiments were performed with a PORE SIZER 9320 (Ghent University).

4. Results and disscussions

4.1. Petrology and mineralogy

Thin section and XRD based petrographic analysis revealed that the samples can be categorized as illite rich and kaolinite rich, based on clay mineralogy. The thin sections studies under the microscope showed that E1 and E2 sandstone are lithic arkose, while E3 and E4 are arkosic sandstones (Fig. 2). All of these sandstone samples contain 40–50 percent of quartz with no considerable variation. Similarly, the total feldspar content ranges between 25–35%, but XRD analysis shows that the ratio of K-feldspar to plagioclase is higher in E3 and E4 than E1 and E2. E3 has the least clay content (2%), while the remaining samples have 4–5% clay content. Illite is the dominant clay type in E1 and E2, while kaolinite is dominant in E3 and E4. E1 and E2 have fewer quantities of ankerite cement, while E3 moderately and E4 is heavily cemented. All of these sandstones are moderately to poorly sorted, where helium porosity ranges between 10–14%. E1, E2 and E4 have finer grain size, while E3 have coarser grain size (Fig. 3a–d). Large amounts of intergranular and dissoluted pores can be seen in E1 and E2 (Fig. 3a, b), whereas fewer microporosity may be present associated with illite (Fig. 3e). In E3 and E4, intergranular pore spaces are reduced by compaction and quartz over growths (Fig. 3c,d) however, extensive

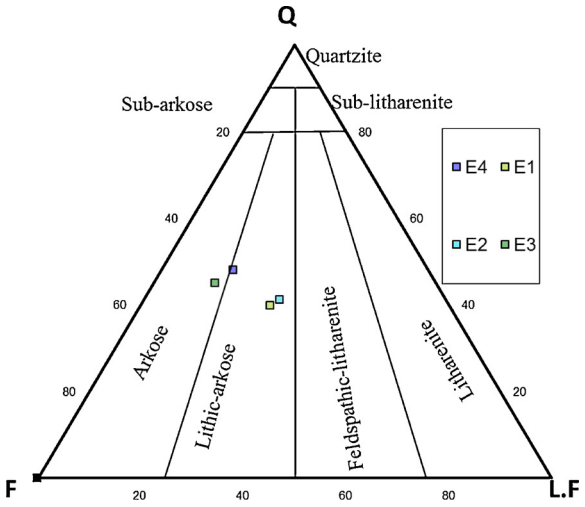

Fig. 2. Ternary diagram showing framework composition of four selected samples from Es3 turbidite sandstone. Samples are plotted according to their relative percent of Quartz (Q), Feldspar (F) and Lithic Fragments (L.F) on three comers of trinary diagram.

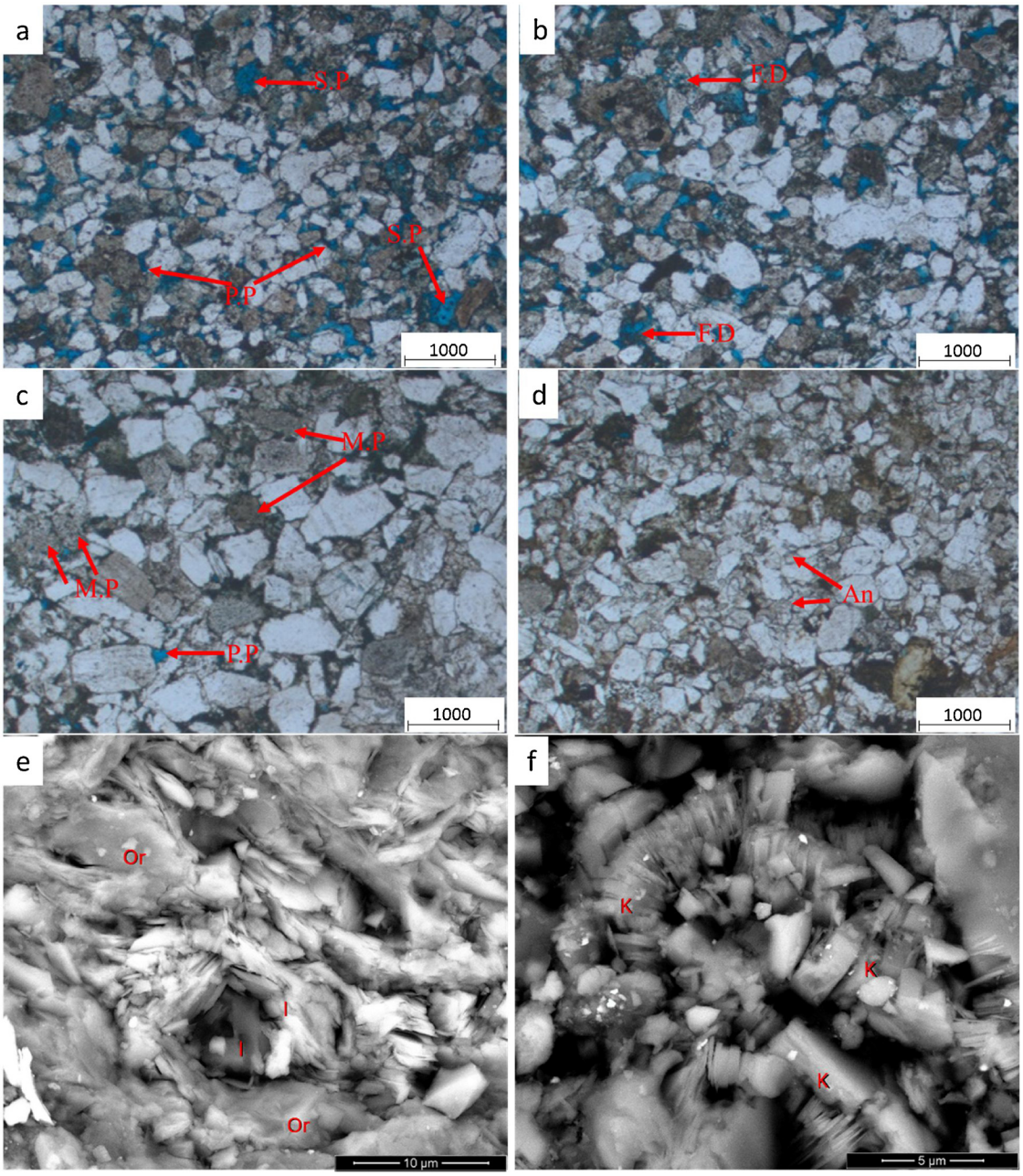

Fig. 3. Thin section and SEM images showing texture and pore geometry of studied samples. (a) E1, high intergranular porosity; (b) E2, high intergranular porosity; (c) E3, Coarse grain, low intergranular porosity; (d) E4, no intergranular porosity, highly cemented by ankerite: (e) Illite clay formed in orthoclase feldspar; (f)typical kaolinite clay structure formed in dissoluted feldspar grain. Note P.P- primary pore, S.P- secondary pore, F.D- dissoluted feldspar, M.P- microporous regions, An- ankerite cement, Or- orthoclase feldspar, I- illite, K- kaolinite.

dissolution and transformation of plagioclase feldspar grains into kaolinite generated microporosity between kaolinite crystals (Fig. 3f).

Distinctive mineral and pore phases can be segmented into 3D labeled volumes based on gray scale histogram. Mineral phase data is also critical to compute petrophysical properties of rock, because wettability and consequently fluid flow largely depends upon mineral surface (Thyne, 2016). The micro-CT images were segmented into four distinctive phases: 1) macroporosity; 2) microporous regions; 3) granular phase and 4) high density cement phase. The macroporosity phase represents pores with sizes greater than the image resolution, while microporous regions are those regions where the pore space cannot be resolved by the given image resolution. Segmentation of above mentioned two categories of porous datasets can be understood as; (1) macropores (100% pores), (2) micropores (linear range from 99% to 1% pore) based on x-rays intensity from micro-CT images. Macroporosity includes intergranular pores and secondary dissolution pores in the plagioclase, while microporous regions usually include pores present in the clay mineral and carbonate cement. The granular phase coarsely represents quartz and feldspars minerals while the high-density cement phase represents carbonate cement and heavy minerals such pyrite and rutile. Calcium and magnesium rich carbonate cement exhibit a higher average atomic number than the quartz and feldspar grains, which can be identified as the brightest phase in the gray value images. Volume fraction of each phase, volume of interest (VOI) and voxel size are given in Table 2.

Table 2
Bulk mineralogy and clay mineralogy of four selected samples of Es3 turbidite sandstone for this study.

Sample	Quartz (%)	Potasium feldspar (%)	Plagioclase (%)	Calcite (%)	Ankerite (%)	Siderite (%)	Pyrite (%)	Clay mineral (%)	Kaolinite (%)	Chlorite (%)	Illite (%)	I/S mixed layer (%)	Smetcite (S) % in I/S
E1	47	7	35	1	3	1	1	5	0	0	69	31	20
E2	57	6	30	–	3	–	–	4	0	0	85	15	20
E3	51	7	22	–	18	–	–	2	50	19	8	23	20
E4	33	7	19	1	36	–	–	4	57	3	11	29	20

4.2. Comparison of mineral data from micro-CT and XRD

The mineral phase data measured in the micro-CT segmented images are correlatable with the mineral content measured using XRD. Although, the measuring method and instrumental principal are different, the results show that a match exist in mineralogy measured by both these techniques for the studied samples. Comparison of these two provides a validation of the micro-CT image segmentation and some additional insights of spatial distribution of minerals and porosity. If quartz and feldspar contents from XRD are added together, the resulting total (Q + F) match the granular phase (G) volume fraction from micro-CT (Fig. 4a). E1 and E2 samples having lesser microporous regions gives a closer match. If we add the microporous regions (Mp) to the granular phase, E1 and E3 give the closest match. This means that most of the microporosity is associated with feldspar content and are present in dissoluted feldspar grains. E4 is heavily cemented where cement has occupied most of the macropores and microporosity exist in clay mixed cement phase. Carbonate cement (Ca + An) contents XRD gives a closer match to high density cement phase (HDC) in E1, E2 and E3 where microporous regions are not present in the cement phase (Fig. 4b). However, when we add microporous regions to the high-density cement phase, E4 gives a closer match meaning that the microporosity in E4 is associated with the cement.

4.3. Pore space analysis from micro-CT images

The multiphase segmentation shows that E3 and E4 have a very low macroporosity, especially in E4 where the macroscopic porosity is almost zero. However, the X-ray datasets of these samples have significant amount of microporous regions. E1 and E2 have significantly higher macroporosity values and the quantity of microporous regions are lesser than E3 and E4. Volume fractions of marcoporosity and microporous regions for each sample are given in Table 3.

In order to investigate impact of microporosity on percolation porosity or connectivity, two binary datasets were created from each sample. The first dataset consisted of macroporosity (zero) and all other phases (one), while in the other dataset, microporous regions was also added to the macroporosity, thus in this binary volume the total porosity equaling the sum of the macroporosity and microporous regions. In this way, we could examine whether a system percolates without the aid of microporosity or microporous region must contribute to flow in order to have a percolating system. Here percolating porosity means volume percent of pores, which are reachable from the inlet.

Considering illite dominated sandstone, E1 has 8.9% macroporosity and 1.7% microporous regions and E2 has 9.7% macroporosity and 1.8% microporous regions (Table 3). However, percolating macroporosity are also very near to macroporosity in these two samples (Table 4). Whereas, 15% of macropores in E1 and 9% in E2 do not contribute to percolation. If microporous regions are taken into account, the percolating porosity improves and percent of pores that don not contribute to percolation decrease and remain less than 5% (Table 4). For E3 and E4, the situation is different, where E3 contains only 3.2% of macropores at a resolution of 1.7 μm, but has no percolating porosity at this resolution. Including the microporous regions, the total porosity reaches to 9.2%, and percolating porosity to 8.6% (Table 4). For E4, that has few visible pores at 1.7 μm resolution, a percolating porosity of 2.4% exists when including the microporous regions in the porosity (Table 4). 2D gray scale image showing mineral segmentation of four samples are present in Fig. 5.

4.4. Pore size distribution (PSD) from MICP

Pore entry radius r_p can be defined as a function of interfacial tension, contact angle, capillary pressure (Alyafei et al., 2015, 2016).

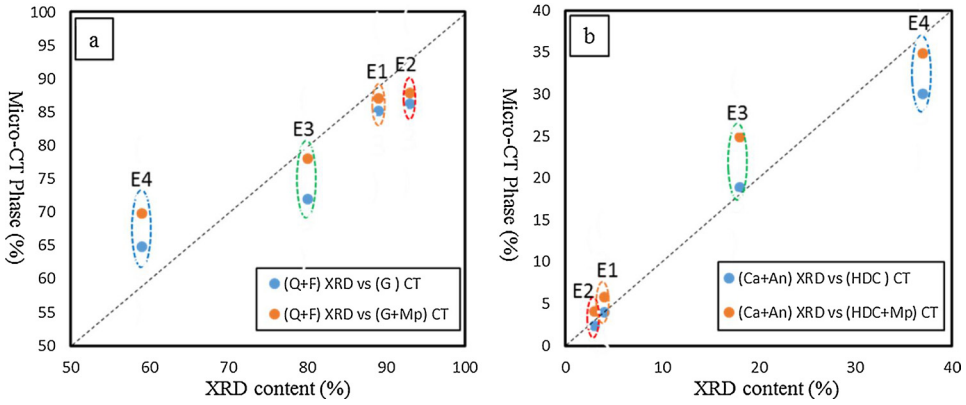

Fig. 4. Comparison of micro-CT mineral phase and XRD mineralogy. (a) Quartz + feldspar vs granular phase and granular phase + microporous phase (Mp); (b) Carbonate cement from XRD vs high density cement phase and high density cement phase + microporous phase. Quartz = Q, feldspar = F, Granular phase = G, microporous phase = Mp, calcite = Ca, Ankerite, = An, high density cement phase = HDC.

Table 3
Statistics of segmented mineral phases from 3D micro-CT images.

Sample	E1	E2	E3	E4
Resolution	1.49 µm	1.49 µm	1.7 µm	1.7 µm
VOI	800 × 800 × 1000 voxels	800 × 800 × 800 voxels	500 × 500 × 350 voxels	400 × 400 × 400voxels
# of phases	4	4	4	4
Macroporosity	9.0%	9.7%	3.2%	0.3%
Microporous regions	1.8%	1.7%	6.0%	4.9%
Granular phase	85.2%	86.2%	72.0%	64.9%
High density (Cement)	4.0%	2.4%	18.9%	30%

$$r_p = \frac{2\partial \cos\theta}{P_c(S_w)}$$

Where P_c is capillary pressure in Pa, ∂ is interfacial tension, 0.48 N/m for a mercury/air system, θ is contact angle, which is 40° for mercury, S_w is water saturation which is assumed as wetting phase.

We used probability distribution function (f) of r_p as described by Dullien (1992) to get PSD.

$$r_p f(r_p) = r_p \frac{dS_w}{dr_p} = -P_c \frac{dS_w}{dP_c} = -\frac{dS_w}{dlnP_c}$$

Fig. 6 shows PSD from MICP analysis, the black vertical line depicts highest image resolution (1.49 µm). PSD from MICP data show that E1 and E2 have unimodal curve with majority of pore size greater than image resolution 1.49 µm (Fig. 6a), while E3 and E4 have bimodal distribution with around half pore size less then image resolution 1.7 µm (Fig. 6b).

4.5. Pore space analysis and connectivity from PNM

PNM were extracted from the segmented datasets of four samples. PNM enable us to calculate the average connectivity (coordination number), and spatial and statistical distribution of pore and throat radii. Pore networks were only extracted from the datasets where only the macropores (100% pore) are present. A 3D representation of pore network can be seen in Fig. 7.

4.5.1. E2

In E2, PNM captured 14180 nodes with average connectivity of 3.9. Minimum connectivity is 0 where pores are completely isolated and a maximum connectivity of 129 probably caused by feldspar dissolution where large number of intragranular pores are in contact with single intergranular pore. Unconnected pores are 982, and the average connectivity among the connected pores is 4.2 (Table 5). The average pore size in E2 is 5.9 µm, and the minimum and maximum pore sizes are 0.7 and 81.9 µm respectively (Table 5).

4.5.2. E1

In E1, PNM extracted 20403 nodes with an average connectivity of 4.2, which is just slightly higher than the E2 connectivity. The pore network has a minimum connectivity of 0 (where pores are completely isolated) and a maximum connectivity of 262 (probably caused by feldspar dissolution where large number of intragranular pores are in contact with single intergranular pore). 1319 pores are unconnected, which is significantly higher than in E2, and the average connectivity among connected pores is 4.46. The average pore size in E1 is 5.7 µm, and the minimum and maximum pore sizes are 0.6 and 31 µm respectively (Table 5).

4.5.2. E4

E4 has a network consisting of only 90 nodes, and an average connectivity is less than 1. With a number of 42 unconnected nodes, this network is almost not-connected. At this resolution, only few macropores are captured from this sample. Such a minor connectivity

Table 4
Showing volume percent of macroporosity and microporous regions with corresponding percolating porosity.

Sample	E1	E2	E3	E4
Resolution	1.49 µm	1.49 µm	1.7 µm	1.7 µm
VOI	800 × 800 × 1000 voxels	800 × 800 × 800 voxels	500 × 500 × 350 voxels	400 × 400 × 400 voxels
Macroporosity	8.9%	9.7%	3.2%	0.3%
Percolating macroporosity	7.6%	8.8%	0%	0%
Macroporosity + microporous regions	10.7%	11.3%	9.2%	5.1%
Percolating porosity when macroporosity + microporous regions	10.2%	10.8%	8.6%	2.4%

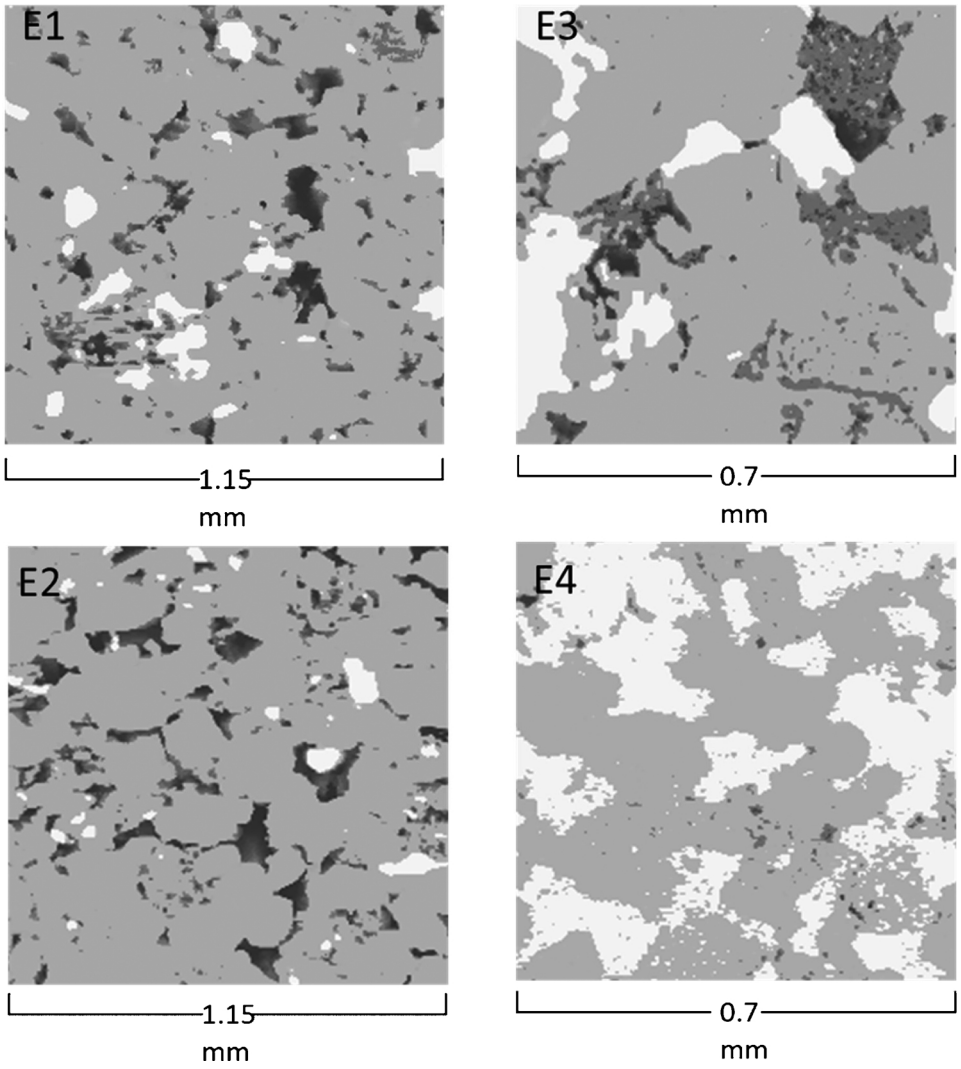

Fig. 5. Segmented four mineral phases represented in 2D images slices. Images are in grayscale; black color represent pore, dark gray microporous, light gray grain phased and white is high density cement phase.

makes this pore network not very representative. The average size of the visible pores is 4 μm, and there were no pores larger than 8 μm present in the analyzed volume (Table 5).

4.5.3. E3

From E3 network 1010 nodes were extracted, with an average connectivity of 2.3% among all pore. Although there are only 196 unconnected pores but average connectivity (2.3) among all pores is comparatively very less than E1 and E2. However, it reaches 2.85 when

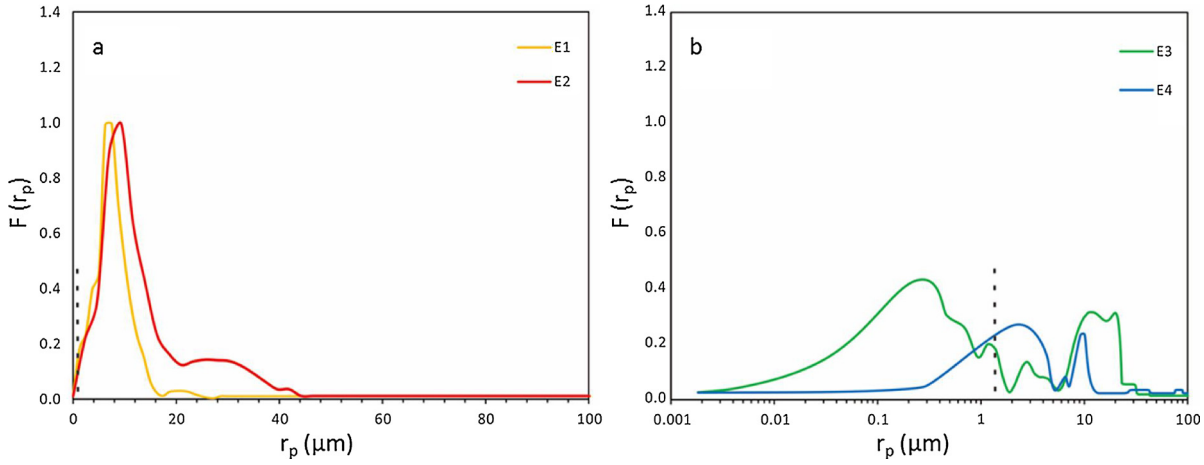

Fig. 6. PSD derived from probability distribution function; (a) E1 and E2; (b) E3 and E4. Note; the dashed line depicts r_p = 1.49 μm (image resolution).

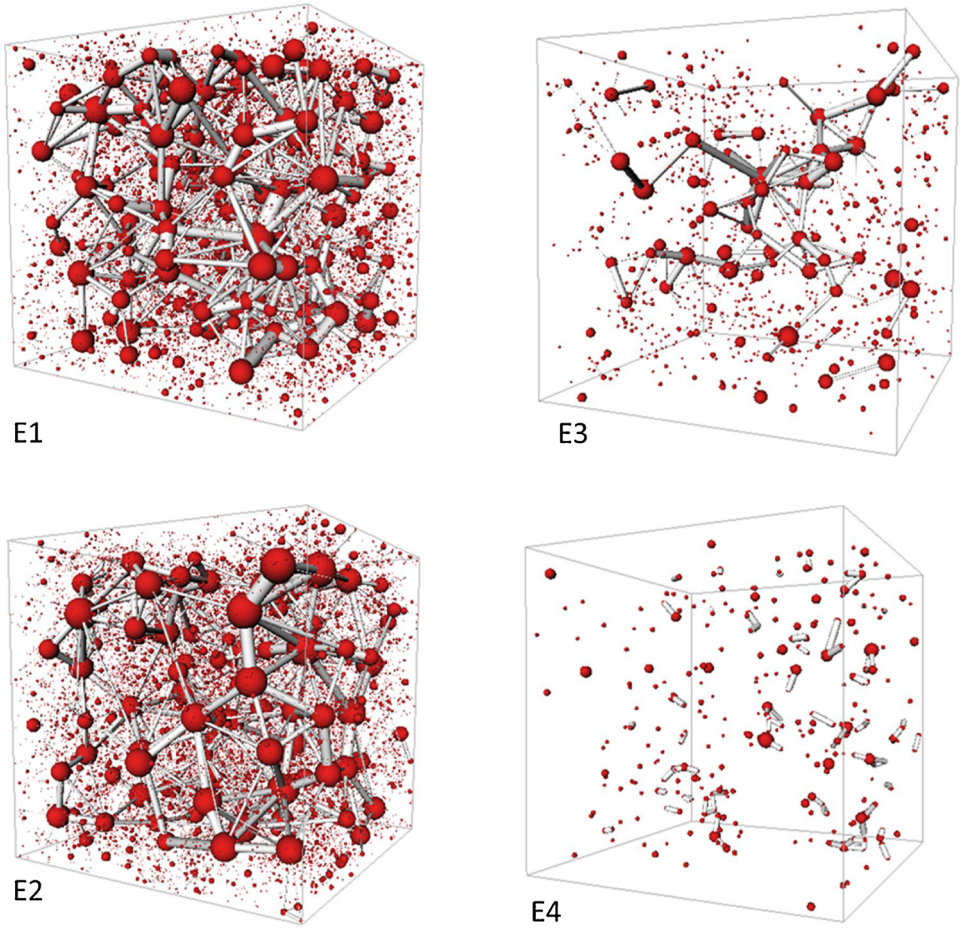

Fig. 7. Showing extracted pore network from segmented micro-CT image of four samples. Sphere represent pore and rod represent throat.

unconnected pores are disregarded. The average pore size of E3 is 6 μm and maximum pore size observed wa 37 μm in this dataset (Table 5).

4.6. Absolute permeability

Absolute permeability was measure on PNM and directly on voxelized image solving strokes equation following darcy,s law. As expected, the absolute permeability of E1 and E2 is greater than 10 mD. While in E3 and E4, it is very near to the value (0.1 mD) which mark a rock as tight reservoir (Table 6). Although, the results are similar but PNM method is giving comparatively higher values of absolute

Table 6
Showing absolute permeability results computed directly on 3D voxelized segmented images and PNM.

Sample	Direct (mD)	PNM (mD)
E1	10.93	12.86
E2	25.42	30.28
E3	0.18	0.26
E4	0.2	

Table 5
Pore network properties; network is extracted from segmented 3D micro-CT image using the grain recognition-based method.

Sample	E1	E2	E3	E4
Resolution	1.5 μm	1.5 μm	1.7 μm	1.7 μm
VOI	800 × 800 × 1000 voxels	800 × 800 × 800 voxels	500 × 500 × 350 voxels	400 × 400 × 400 voxels
Network porosity	8.7%	9.5%	2.9%	0.1%
Number of pores	20403	14180	1010	90
Average pore radius (μm)	5.7	5.9	6.1	4
Min. Pore radius (μm)	0.6	0.7	1.1	1.4
Max Pore radius (μm)	30.9	81.9	37.6	8.2
Average throat radius (μm)	4.0	4.1	4.5	2.9
Min. throat radius (μm)	0.55	0.50	0.30	0.30
Max throat radius (μm)	21.73	28.89	25.38	6.3
Average connectivity	4.2	3.9	2.3	1
Minimum connectivity	0	0	0	0
Maximum connectivity	262	129	34	5
Unconnected nodes	1319	982	196	42
Avg. Connectivity disregarding unconnected nodes	4.5	4.2	2.85	1.8

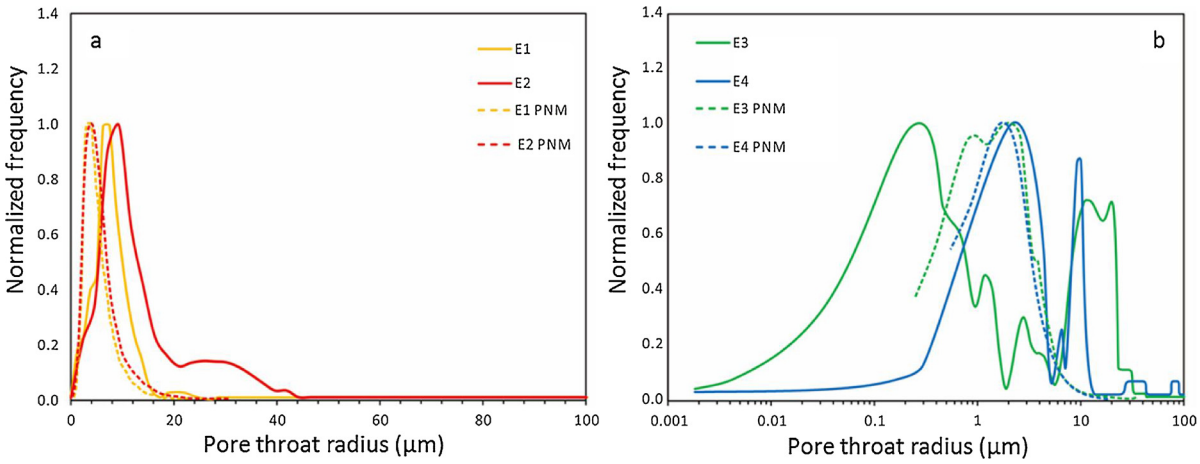

Fig. 8. A comparison of throat radius distribution from MICP and extracted PNM; (a) E1 and E2; (b) E3 and E4.

permeability, which is due to simpler nature of PNM. The similarity in results indicate that PNM did enough to capture the details of pore space. Absolute permeability cannot be measured on E4 sample, because the PNM of this sample is not connected.

4.7. Comparison of PSD from MICP and PNM

MICP can mathematical describe the pore-throat system in the form of bundles of capillaries, thus it does not take account of tortuosity, wettability, connectivity (coordination number) and shape factor, whereas, micro-CT based PNM analysis offer pore geometry, the length of throats and connectivity (coordination number), which are significant parameters for flow modeling in porous media (Pittman, 1992; Ortega and Aguilera, 2014). In agreement to MICP, the shape and width of the PSD curve from PNM of E1 and E2 are very similar to each other (Fig. 8a). However, the peak widths of these curves are smaller than MICP and position of peak is shifted towards left. The PSD curve from PNM of E3 is semi-bimodal and E4 is unimodal (Fig. 8b). Both of these curves are uncompleted from left side. The peak width and specially the peak positions does not match well with MICP curves. The uncompletedness of curve in E3 and E4 typically and lack of agreement of curves in all samples generally represents the disability of micro-CT images to capture whole pore space. However, it is worth mentioning here that disagreement can also exist due to some discrepancies in MICP data. The discrepancies are; (1) surface irregularities of sample also result in extra throat volume (2) PSD data from MICP is unreliable at pressures 70 MPa and above (Cao et al., 2016a,b) because, under such a pressure the pore structure can change, grains can breakdown and the opening of small closed pores can occur.

4.8. Implication for petroleum reservoir

In sandstone, macropores are located in intergranular space a narrow connection (throat) usually exists along grain boundaries between these pores. Theocratically, grain packing models such as Finney's packing (Finney, 1970), the average connectivity of a pore should be four. However, cementation and ductile deformation can partially block pore and pore throats ultimately reducing average connectivity which becomes less than four (Mousavi and Bryant, 2012). E1 and E2 shows excellent connectivity of macropores even the microporous regions are not included in pore network. Fig. 9 show that highest frequency occurs at a coordination number value of 4. Even the image porosity, pore network porosity and MICP porosity are similar (Table 7), this means macropores are well connected and retains most of the porosity volume. In such simple homogeneous rocks, single imaging scale is enough to represent pore space for accurate rock model. The PNM extracted from single resolution image from micro-CT can accurately predict flow properties in these rocks (Jiang et al., 2013; Bultreys et al., 2016b).

Micropores are located in dissoluted feldspar grains and clay mineral which are resultant of feldspar dissolution. In E3, compaction, quartz overgrowth and existence of microporous regions reduced connectivity of macropores. While, in E4 heavy ankerite cementation resulted in least connectivity values of macropores. The highest frequency of coordination number is at 1 in E4 and at 2 in E3 sample (Fig. 9). In E3 and E4, image porosity and pore network porosity are far less than MICP porosity (Table 7) which means large amount of micropores lies below image resolution. Penetration of mercury to these micropores is somehow evidence of connectivity, this leads to the point that these pores can contribute to displacement process but insanely high pressures are required for non-wetting phase to enter these pores. Some researchers neglect microporosity by assuming that it is poorly connected and does not contribute to relative permeability is especillay in hydrocarbon reservoir rock (Gharbi and Blunt, 2012). In fact, microporosity does not take part in displacement process and remains water filled contributing to irreducible water saturation (Blunt et al., 2002; Øren and Bakke, 2002).

However, finding out the effective pore throat system that dominates flow in these rocks is crucial. The effective set of pore throat system (r35) that dominates flow in a reservoir rocks corresponded to a mercury saturation of 35% (Winland, 1972). For samples used in this study, r35 lies below the image resolution, whereas the average pore-throat radius (volume weighted) in E1 and E2 is almost same as image resolution (Table 7). The minimum predicted throat radii by PNM lies very near to r35 in E1 and E2. Most interestingly, it matches closely with mean r35 from 312 Winland samples. This means the model from E1 and E2 can behave well to simulate flow properties. The minimum predicted throat radii by PNM is double than r35 from MICP and higher than mean r35 from Winland samples. This means the considerable porosity is not detected by micro-CT image, which is necessary to be incorporated into model to get reliable flow simulations results.

Although, multiscale modeling is out of the scope of this study, but it is worth mentioning here that the rocks like E3 and E4, which have considerable microporosity cannot be represented in single scale PNM. Multiscale network modeling is needed to integrate macropore and micropore into single PNM (Bultreys et al., 2016b; Prodanović et al., 2015). Micro-CT cannot detect micropores as a void space, but it can be represented theoretically in the models. Bultreys et al. (2015) developed micro-CT based dual pore network model (DPNM) which includes microporosity by adding symbolic micro-links, while treating the macroporosity as a traditional PNM. A deterministic network model based on synthetic granular media was developed by Mehmani and

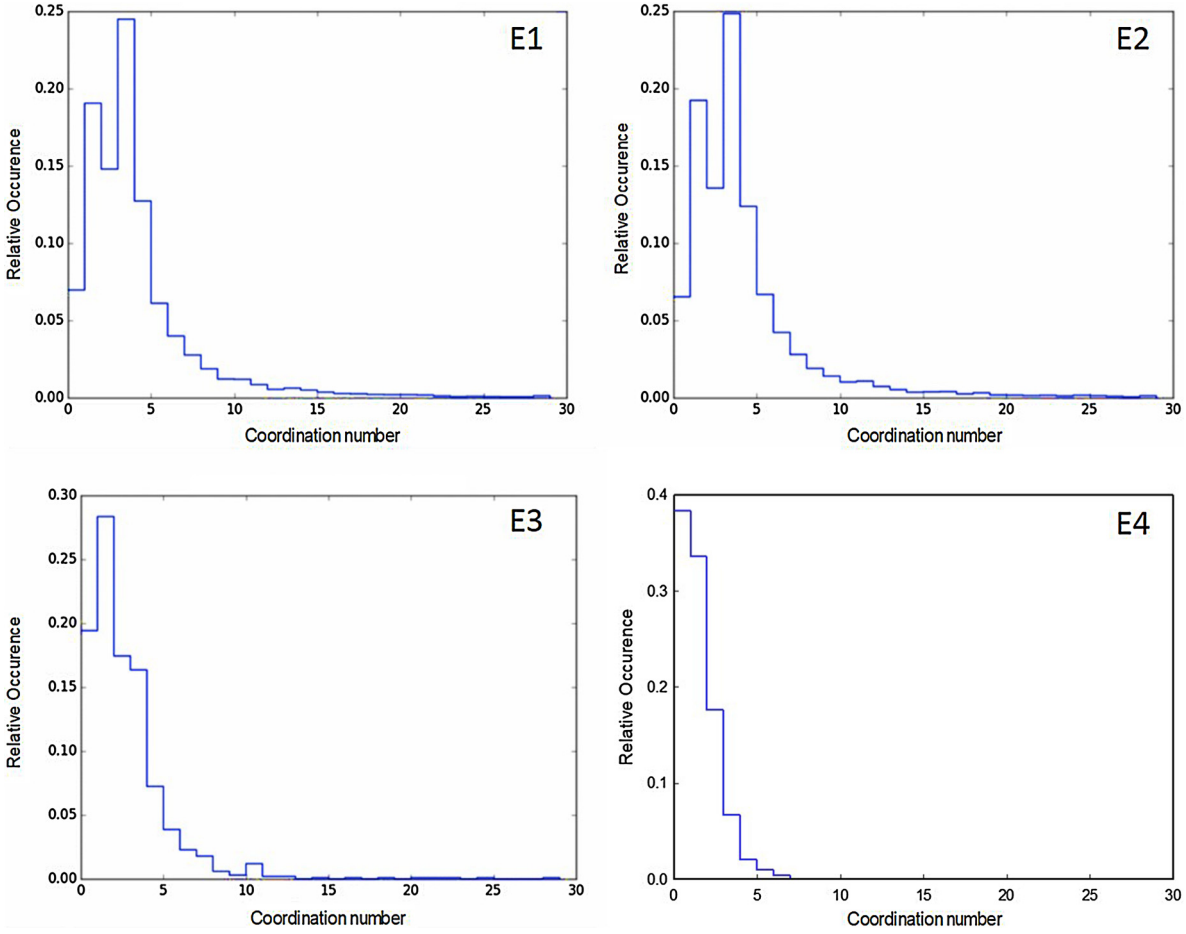

Fig. 9. Histogram showing connectivity pore in four studied samples in the form of coordination number.

Table 7
A comparison of pore space analysis from segmented micro-CT image, extracted network and MICP.

Sample	MICP			Micro-CT		Extracted Pore network		
	Porosity (%)	Aver. throat radius (μm)	r35 (μm)	Macro porosity (%)	Micro porous regions (%)	Porosity (%)	Min. throat radius (μm)	Aver. throat radius (μm)
E1	8.7	1.46	0.35	8.9	1.8	8.7	0.55	4.0
E2	9.36	1.56	0.51	9.7	1.7	9.5	0.50	4.1
E3	6.09	0.94	0.17	3.2	6	2.9	0.30	4.5
E4	0.83	0.29	0.11	0.3	4.9	0.1	0.30	2.9

Prodanović (2014a). In this model, micropores and macropores were attached together in a sense that the extent, location and degree of each diagenetic process was a controlled parameter. Further, this modeling is extended to imaged natural rocks (Prodanović et al., 2015; Bultreys et al., 2016b). Such kind of multiscale and objective oriented modeling is a possible solution of tight rocks which bear multi-scale pore system.

5. Conclusions

Micro structures in natural rock are complex in nature and spread across several scales. A preliminary study of thin-sections can provide a better idea about location and extent of macro and micropores. Furthermore, XRD analysis are not only helpful to validate segmentation but a comparison of mineralogical data from segmented micro-CT images and XRD also provide valuable insights about distribution of microporosity among different phases. It is clearly evident from MICP data that considerable amount of pore space (microporosity) is present below image resolution in E3 and E4 which is mainly associated with kaolinite clay and clay mixed carbonate cement. But majority of the pore space is captured by micro-CT and there is no considerable microporosity present in E1 and E2. Similarity in absolute permeability results calculated on PNM and directly voxelized image reflects the ability of PNM to capture enough details of pore space. The throat distribution from PNM does not match completely with MICP, however a better agreement exists in E1 and E2 but poor and confusing agreement exist in E3 and E4. The lack of agreement between prediction and lab experimental exist due to resolution limitation in micro-CT. The studied PNM behave well and are reliable for pore scale simulation in E1 and E2 where pore space vastly captured by micro-CT images and the minimum throat size from PNM lies near to r35. Whereas, the pore scale simulations cannot be considered as reliable where pore space is not fully captured and a big gap lies in minimum throat radius from PNM and r35.

Acknowledgements

The work has been financially supported by the ‘China Scholarship Council’ and ‘National Science and Technology, P.R. China’ Project

(Special Grant No. 2016ZX05027004-002 and 41672129). Special thanks to Geosciences Institute of the Shengli Oilfield, SinoPec for providing us cores samples for this study. Authors are also grateful to Dr. Nayef Alyafei (Texas A&M University at Qatar, Qatar), Dr. Theis I. Solling (University of Copenhagen, Denmark), and Dr. Macunfei (China University of Petroleum, Qingdao) for their positive suggestions and improving this manuscript.

References

Alyafei, N., Raeini, A.Q., Paluszny, A., Blunt, M.J., 2015. A sensitivity study of the effect of image resolution on predicted petrophysical properties. Transp. Porous Media 110, 157–169. http://dx.doi.org/10.1007/s11242-015-0563-0.

Alyafei, N., Mckay, T.J., Solling, T.I., 2016. Characterization of petrophysical properties using pore-network and lattice-Boltzmann modelling: choice of method and image sub-volume size. J. Pet. Sci. Eng. 145, 256–265. http://dx.doi.org/10.1016/j.petrol.2016.05.021.

Andra, H., Combaret, N., Dvorkin, J., Glatt, E., Han, J., Kabel, M., Keehm, Y., Krzikalla, F., Lee, M., Madonna, C., Marsh, M., Mukerji, T., Saenger, E.H., Sain, R., Saxena, N., Ricker, S., Wiegmann, A., Zhan, X., 2013. Digital rock physics benchmarks? Part I Imaging and segmentation. Comput. Geosci. 50, 25–32. http://dx.doi.org/10.1016/j.cageo.2012.09.005.

Arns, C.H., 2004. A comparison of pore size distributions derived by NMR and X-ray-CT techniques. Physica A: Statistical Mechanics and Its Applications. pp. 159–165. http://dx.doi.org/10.1016/j.physa.2004.03.033.

Bakke, S., Øren, P.-E., 1997. 3-D pore-scale modelling of sandstones and flow simulations in the pore networks. Soc. Pet. Eng. 2, 136–149 (SPE 35479).

Blunt, M.J., Jackson, M.D., Piri, M., Valvatne, P.H., 2002. Detailed physics, predictive capabilities and macroscopic consequences for pore-network models of multiphase flow. Adv. Water Resour. 25, 1069–1089. http://dx.doi.org/10.1016/S0309-1708(02)00049-0.

Bouma, A.H.A., 2000. Fine-grained, Mud-rich Turbidite Systems: Model and Comparison with Coarse-grained, Sand-rich Systems. Spec. Publ. pp. 9–19. http://dx.doi.org/10.1144/GSL.SP.2004.222.01.02.

Bultreys, T., Van Hoorebeke, L., Cnudde, V., 2015. Multi-scale, micro-computed tomography-based pore network models to simulate drainage in heterogeneous rocks. Adv. Water Resour. 78, 36–49. http://dx.doi.org/10.1016/j.advwatres.2015.02.003.

Bultreys, T., De Boever, W., Cnudde, V., 2016a. Imaging and image-based fluid transport modeling at the pore scale in geological materials: a practical introduction to the current state-of-the-art. Earth-Sci. Rev. 155, 93–128. http://dx.doi.org/10.1016/J.EARSCIREV.2016.02.001.

Bultreys, T., Stappen, J., Van Kock, T., De Boever, W., De Boone, M.A., Hoorebeke, L., Van Cnudde, V., 2016b. Investigating the relative permeability behavior of microporosity-rich carbonates and tight sandstones with multiscale pore network models. J. Geophys. Res. Solid Earth 121, 7929–7945. http://dx.doi.org/10.1002/2016JB013328.

Cao, Z., Liu, G., Kong, Y., Wang, C., Niu, Z., Zhang, J., Geng, C., Shan, X., Wei, Z., 2016a. Lacustrine tight oil accumulation characteristics: Permian Lucaogou Formation in Jimusaer Sag, Junggar Basin. Int. J. Coal Geol. 153, 37–51. http://dx.doi.org/10.1016/J.COAL.2015.11.004.

Cao, Z., Liu, G., Zhan, H., Li, C., You, Y., Yang, C., Jiang, H., 2016b. Pore structure characterization of Chang-7 tight sandstone using MICP combined with N 2 GA techniques and its geological control factors. Sci. Rep. http://dx.doi.org/10.1038/srep36919.

Cid, H.E., Carrasco-Núñez, G., Manea, V.C., 2017. Improved method for effective rock microporosity estimation using X-ray microtomography. Micron 97, 11–21. http://dx.doi.org/10.1016/j.micron.2017.01.003.

Cnudde, V., Boone, M.N., 2013. High-resolution X-ray computed tomography in geosciences: a review of the current technology and applications. Earth-Sci. Rev. http://dx.doi.org/10.1016/j.earscirev.2013.04.003.

De Boever, W., Derluyn, H., Van Loo, D., Van Hoorebeke, L., Cnudde, V., 2015. Data-fusion of high resolution X-ray CT, SEM and EDS for 3D and pseudo-3D chemical and structural characterization of sandstone. Micron 74, 15–21. http://dx.doi.org/10.1016/j.micron.2015.04.003.

Dong, H., Blunt, M.J., 2009. Pore-network extraction from micro-computerized-tomography images. Phys. Rev. E – Stat. Nonlinear, Soft Matter Phys. 80, 1–11. http://dx.doi.org/10.1103/PhysRevE.80.036307.

Dullien, F.A., 1992. Porous Media: Fluid Transport and Pore Structure, 2nd ed. Academic Press, NewYork.

Elgmati, M., Bai, B., 2011. Shale gas rock characterization and 3D submicron pore network reconstruction. Geol. Sci. Eng. 90 Master of.

Feng, Y., Li, S., Lu, Y., 2013. Sequence stratigraphy and architectural variability in late eocene lacustrine strata of the dongying depression, Bohai Bay Basin, Eastern China. Sediment. Geol. 295, 1–26. http://dx.doi.org/10.1016/j.sedgeo.2013.07.004.

Finney, J.L., 1970. Random packings and the structure of simple liquids I. The geometry of random close packing. Proc. R. Soc. A Math. Phys. Eng. Sci. 319, 479–493. http://dx.doi.org/10.1098/rspa.1970.0189.

Gharbi, O., Blunt, M.J., 2012. The impact of wettability and connectivity on relative permeability in carbonates: a pore network modeling analysis. Water Resour. Res. 48. http://dx.doi.org/10.1029/2012WR011877.

Golab, A.N., Knackstedt, M.A., Averdunk, H., Senden, T., Butcher, A.R., Jaime, P., 2010. 3D porosity and mineralogy characterization in tight gas sandstones. Lead. Edge. http://dx.doi.org/10.1190/1.3525363.

Jiang, Z., Van Dijke, M.I.J., Sorbie, K.S., Couples, G.D., 2013. Representation of multi-scale heterogeneity via multiscale pore networks. Water Resour. Res. 49, 5437–5449. http://dx.doi.org/10.1002/wrcr.20304.

Knackstedt, M., Arns, C., 2007. Archie's exponents in complex lithologies derived from 3D digital core analysis. SPWLA 48th Annual Logging Symposium 1–16.

Knackstedt, M., Carnerup, A., Golab, A., Sok, R., Young, B., Riepe, L., 2013. Petrophysical characterization of unconventional reservoir core at multiple scales. Petrophysics 54, 216–223. http://dx.doi.org/10.1190/urtec2013-160.

Liu, J., Xian, B., Wang, J., Ji, Y., Lu, Z., Liu, S., 2017. Sedimentary architecture of a sub-lacustrine debris fan: eocene dongying depression, Bohai Bay Basin, East China. Sediment. Geol. 362, 66–82. http://dx.doi.org/10.1016/J.SEDGEO.2017.09.014.

Manwart, C., Aaltosalmi, U., Koponen, A., Hilfer, R., Timonen, J., 2002. Lattice-Boltzmann and finite-difference simulations for the permeability for three-dimensional porous media. Phys. Rev. E – Stat. Phys. Plasmas Fluids Relat. Interdiscip. Top. 66. http://dx.doi.org/10.1103/PhysRevE.66.016702.

Marquez Ceballos, X., Solling, T., Finlay, S., Bounoua, N., Gagigi, T., 2014. 3D imaging of porosity modifying phases in shuaiba reservoir, Al Shaheen field. International Petroleum Technology Conference. http://dx.doi.org/10.2523/IPTC-17672-MS.

Masschaele, B., Dierick, M., Loo, D., Van Boone, M.N., Brabant, L., Pauwels, E., Cnudde, V., Van Hoorebeke, L., 2013. HECTOR: A 240 kV micro-CT setup optimized for research. J. Phys. Conf. Ser. 463, 12012. http://dx.doi.org/10.1088/1742-6596/463/1/012012.

Mehmani, A., Prodanović, M., 2014a. The application of sorption hysteresis in nano-petrophysics using multiscale multiphysics network models. Int. J. Coal Geol. 128–129, 96–108. http://dx.doi.org/10.1016/j.coal.2014.03.008.

Mehmani, A., Prodanović, M., 2014b. The effect of microporosity on transport properties in porous media. Adv. Water Resour. 63, 104–119. http://dx.doi.org/10.1016/j.advwatres.2013.10.009.

Mousavi, M.A., Bryant, S.L., 2012. Connectivity of pore space as a control on two-phase flow properties of tight-gas sandstones. Transp. Porous Media 94, 537–554. http://dx.doi.org/10.1007/s11242-012-0017-x.

Øren, P.E., Bakke, S., 2002. Process based reconstruction of sandstones and prediction of transport properties. Transp. Porous Media 46, 311–343. http://dx.doi.org/10.1023/A:1015031122338.

Ortega, C., Aguilera, R., 2014. A complete petrophysical evaluation method for tight formations from drill cuttings on in the absence of well logs. SPE J. 19, 636–647.

Piri, M., Blunt, M.J., 2005. Three-dimensional mixed-wet random pore-scale network modeling of two- and three-phase flow in porous media. II. Results. Phys. Rev. E 71, 26302. http://dx.doi.org/10.1103/PhysRevE.71.026302.

Pittman, E.D., 1992. Relationship of porosity and permeability to various parameters derived from mercury injection-capillary pressure curves for sandstone. Am. Assoc. Pet. Geol. Bull. http://dx.doi.org/10.1017/CBO9781107415324.004.

Prodanović, M., Mehmani, A., Sheppard, A.P., 2015. Imaged-based multiscale network modelling of microporosity in carbonates. Geol. Soc. Lond. Spec. Publ. 406, 95–113. http://dx.doi.org/10.1144/SP406.9.

Schlüter, S., Sheppard, A., Brown, K., Wildenschild, D., 2014. Image processing of multiphase images obtained via X-ray microtomography: a review. Water Resour. Res. http://dx.doi.org/10.1002/2014WR015256.

Shanmugam, G., 2002. Ten turbidite myths. Earth-Sci. Rev. 58, 311–341. http://dx.doi.org/10.1016/S0012-8252(02)00065-X.

Solling, T., Marquez, X., Finlay, S.J., Bounoua, N., Gagigi, T., McKay, T., Fogden, A., 2014. 3D imaging of the pore network in the Shuaiba Reservoir, Al Shaheen field. International Petroleum Technology Conference. http://dx.doi.org/10.2523/IPTC-17673-MS.

Teles, A.P., Lima, I., Lopes, R.T., 2016. Rock porosity quantification by dual-energy X-ray computed microtomography. Micron 83, 72–78. http://dx.doi.org/10.1016/J.MICRON.2016.02.004.

Thyne, G., 2016. Wettability alteration in reservoirs: how it applies to Alaskan oil production. In: The SPE Western Regional Meeting held in Anchorage. Society of Petroleum Engineers. http://dx.doi.org/10.2118/180370-MS.

Valvatne, P.H., Blunt, M.J., 2004. Predictive pore-scale modeling of two-phase flow in mixed wet media. Water Resour. Res. 40. http://dx.doi.org/10.1029/2003WR002627.

Wang, J.D., Li, S.Z., Santosh, M., Dai, L.M., Suo, Y.H., Yu, S., Zhao, S.J., Liu, B., Wang, Q.J., 2013. Lacustrine turbidites in the Eocene Shahejie Formation, Dongying Sag, Bohai Bay Basin, North China Craton. Geol. J. 48, 561–578. http://dx.doi.org/10.1002/gj.2517.

Winland, H.D., 1972. Oil Accumulation in Response to Pore Size Changes, Weyburn Field. Saskatchewan: Amoco Production Company Report.

Zhang, S.W., 2004. The application of an integrated approach in exploration of lacustrine turbidites in Jiyang Sub-basin, Bohai Bay Basin. Chin. J. Pet. Sci. Eng. 41, 67–77. http://dx.doi.org/10.1016/S0920-4105(03)00144-X.